

# Is different $\Lambda$ and $\bar{\Lambda}$ polarization caused by different spatio-temporal freeze-out picture?

O. Vitiuk<sup>1,2</sup>, L.V. Bravina<sup>1\*</sup>, E.E. Zabrodin<sup>1,3</sup>

<sup>1</sup> *Department of Physics, University of Oslo, PB 1048 Blindern, N-0316 Oslo, Norway*

<sup>2</sup> *Taras Shevchenko National University of Kyiv, UA-01033 Kyiv, Ukraine*

<sup>3</sup> *Skobel'tzyn Institute for Nuclear Physics, Moscow State University, RU-119899 Moscow, Russia*

## Abstract

Thermal vorticity in non-central Au+Au collisions at energies  $7.7 \leq \sqrt{s} \leq 62.4$  GeV is calculated within the UrQMD transport model. Tracing the  $\Lambda$  and  $\bar{\Lambda}$  hyperons back to their last interaction point we were able to obtain the temperature and the chemical potentials at the time of emission by fitting the extracted bulk characteristics of hot and dense medium to statistical model of ideal hadron gas. Then the polarization of both hyperons was calculated. The polarization of  $\Lambda$  and  $\bar{\Lambda}$  increases with decreasing energy of nuclear collisions. The stronger polarization of  $\bar{\Lambda}$  is explained by the different space-time distributions of  $\Lambda$  and  $\bar{\Lambda}$  and by different freeze-out conditions of both hyperons.

**PACS:** 25.75.-q, 24.10.Lx, 24.10.Pa

**Keywords:** relativistic heavy-ion collisions, vorticity, polarization, transport models

## 1. Introduction

Experiments with heavy-ion collisions at relativistic and ultrarelativistic energies aim to study properties of very hot and dense nuclear matter, most likely, quark-gluon plasma (QGP) [1]. It is generally believed that in the nuclear matter phase diagram the curve, corresponding to first-order phase transition between the QGP and hadronic matter, ends up (with rising bombarding energy) in a tricritical point, where the transition becomes of second order. Above this energy one is dealing with the crossover type of the phase transition. The latter corresponds to conditions emerging in heavy-ion collisions at top RHIC ( $\sqrt{s} = 200$  GeV) and LHC ( $\sqrt{s} = 2.76$  TeV and 5.02 TeV) energies. Searching for the tricritical point is one of the goals of Beam Energy Scan (BES) program at RHIC, studies of Pb+Pb collisions at SPS CERN, and future experiments on coming soon facilities NICA at JINR and FAIR at GSI.

Non-central heavy-ion collisions generate enormous orbital angular momenta of order up to  $10^5 \hbar$ . Thus, the created QGP should possess extremely high vorticity, that can be probed by global polarization of hyperons, such as  $\Lambda$  or  $\bar{\Lambda}$ . The idea connecting vorticity of QGP fluid with hyperon polarization was put forward in [2]. Nowadays it

becomes a very popular branch of researches in heavy-ion collisions, see, e.g., [3–23] and references therein. Mean-time, STAR Collaboration has observed a very peculiar behavior in polarization of  $\Lambda$  and  $\bar{\Lambda}$  in semi-peripheral gold-gold collisions at center-of-mass energies between 7.7 GeV and 200 GeV. It is well known that polarization of both,  $\Lambda$  and  $\bar{\Lambda}$ , at  $\sqrt{s} = 200$  GeV is consistent with zero [24]. Recently, similar result for the polarization of both hyperons in Pb+Pb collisions at  $\sqrt{s} = 2.76$  TeV and 5.02 TeV was reported by ALICE Collaboration [25]. However, the polarization steadily increases to 2% with reducing c.m. energy to  $\sqrt{s} = 7.7$  GeV. Meanwhile, polarization of  $\bar{\Lambda}$  at  $\sqrt{s} > 7.7$  GeV is a bit larger although consistent within the error bars with that of  $\Lambda$ . But at  $\sqrt{s} = 7.7$  GeV it suddenly rises up to  $(8.3 \pm 3)\%$  [26]. In contrast, in kinetic and hydrodynamic models polarizations of  $\Lambda$  and  $\bar{\Lambda}$  are essentially the same [11, 15, 16, 20, 22, 23]. To explain the difference in polarizations of both hyperons in heavy-ion collisions at intermediate and low energies the anomalous mechanism related to axial vortical effect has been invoked in [13, 14]. Another possibility discussed in [21] is the interaction between the spins of (anti)hyperons and the vorticity of the baryon current.

In the present paper we argue that the difference in  $\Lambda$  and  $\bar{\Lambda}$  polarizations can originate from the different space-time distributions and different freeze-out conditions of both hyperons. The UrQMD model [27, 28] is

\*Corresponding author

Email address: larissa.bravina@fys.uio.no  
(L.V. Bravina<sup>1</sup>)

employed to investigate polarization of  $\Lambda$  and  $\bar{\Lambda}$  hyperons in non-central Au+Au collisions in the energy range  $7.7 \leq \sqrt{s} \leq 62.4$  GeV. The model permits us to trace the history of each hadron back to the last inelastic (chemical freeze-out) or elastic (thermal freeze-out) collision. After that one can investigate the conditions of local equilibrium in a given area of the phase space and extract temperature  $T$ , baryon chemical potential  $\mu_B$ , and strangeness chemical potential  $\mu_S$ . Details of this procedure are discussed in Sec. 2. Section 3 describes the model used to determine the polarization of  $\Lambda$  and  $\bar{\Lambda}$ . Results of our study are presented in Sec. 4. In particular, we show that differences in  $\Lambda$  and  $\bar{\Lambda}$  polarization can be linked to different space-time freeze-out conditions for both types of hyperons, because various areas of the expanding fireball possess different vorticities at different times. Finally, conclusions are drawn in Sec. 5.

## 2. UrQMD and statistical model of ideal hadron gas

Relaxation of hot and dense nuclear matter produced in relativistic heavy-ion collisions to local chemical and thermal equilibrium within in microscopic transport models was studied in, e.g., [29–34]. The method suggested there to determine temperature and chemical potentials of hot and dense medium is as follows. The whole volume of the collision is subdivide into relatively small cells. After the generation of appropriately high number of collisions at the same c.m. energy and with the same centrality, one can extract energy density  $\varepsilon$ , net baryon density  $\rho_B$ , and net strangeness density  $\rho_S$ . In equilibrium, the properties of mixture of hadron species are determined by the set of distribution functions (in system of natural units of  $c = \hbar = k_B = 1$ )

$$f(p, m_i) = \left[ \exp\left(\frac{\epsilon_i - \mu_i}{T}\right) \pm 1 \right]^{-1} \quad (1)$$

Here  $p$  is the momentum,  $m$  is the mass,  $\epsilon_i = \sqrt{p^2 + m_i^2}$  is the energy, and  $\mu_i$  is the chemical potential of the hadron specie  $i$ , respectively. The sign  $-$  stands for bosons and the  $+$  is for fermions. We will consider baryon and strangeness chemical potentials and disregard electric chemical potential, which is usually much smaller than the first two ones. Therefore, the total chemical potential of the  $i$ -th hadron with the baryon charge  $B$  and strange charge  $S$  reads

$$\mu_i = B_i \mu_B + S_i \mu_S \quad (2)$$

The first and the second moments of the distribution function provide us the particle number density  $n_i$  and the energy density  $\varepsilon_i$ , respectively

$$n_i = \frac{g_i}{(2\pi)^3} \int f(p, m_i) d^3 p \quad (3)$$

$$\varepsilon_i = \frac{g_i}{(2\pi)^3} \int \epsilon_i f(p, m_i) d^3 p \quad (4)$$

with  $g_i$  being the spin-isospin degeneracy factor. In order to obtain  $T$ ,  $\mu_B$  and  $\mu_S$  one has to insert the extracted microscopic parameters  $\{\varepsilon^{mic}, \rho_B^{mic}, \rho_S^{mic}\}$  into the system of nonlinear equations

$$\rho_B^{mic} = \sum_i B_i n_i(T, \mu_B, \mu_S), \quad (5)$$

$$\rho_S^{mic} = \sum_i S_i n_i(T, \mu_B, \mu_S), \quad (6)$$

$$\varepsilon^{mic} = \sum_i \varepsilon_i(T, \mu_B, \mu_S), \quad (7)$$

Note that the set of hadron species employed in the SM must be identical to that of the microscopic model. Comparison of hadron yields and energy spectra, given by the microscopic model, to the SM spectra in the central area of heavy-ion collisions has revealed that hot and dense nuclear matter needed about 6 – 8 fm/c to reach the vicinity of chemical and local equilibrium. The extracted temperature will be used for calculation of vorticity of nuclear matter. This issue is discussed in Sec. 3.

## 3. Calculation of vorticity and $\Lambda$ , $\bar{\Lambda}$ polarization

There are several approaches to the vorticity problem in heavy-ion collisions. The most popular is the treatment based on the assumption of local thermal equilibrium at the system freeze-out [8]. Another mechanism is the axial charge separation due to the chiral vortical effect [13]. In the present paper we will follow Refs. [8, 15]. If the system is in local equilibrium and the concentration of both,  $\Lambda$  and  $\bar{\Lambda}$ , is very small, their ensemble averaged spin 4-vector at space-time point  $x$  reads

$$S^\mu(x, p) = -\frac{1}{8m} \epsilon^{\mu\nu\rho\sigma} p_\nu \varpi_{\rho\sigma}(x), \quad (8)$$

containing the hyperon mass  $m$ , antisymmetric tensor  $\epsilon^{\mu\nu\rho\sigma}$ , and the thermal vorticity tensor

$$\varpi_{\mu\nu} = \frac{1}{2} (\partial_\nu \beta_\mu - \partial_\mu \beta_\nu) \quad (9)$$

Here  $\beta^\mu = u^\mu/T$  is the inverse-temperature four-velocity,  $u^\mu$  is hydrodynamic four-velocity and  $T$  is a proper temperature, respectively. Decomposing the thermal vorticity

into the space-time components,

$$\varpi_T = (\varpi_{0x}, \varpi_{0y}, \varpi_{0z}) = \frac{1}{2} \left[ \nabla \left( \frac{\gamma}{T} \right) + \partial_t \left( \frac{\gamma \mathbf{v}}{T} \right) \right] \quad (10)$$

$$\varpi_S = (\varpi_{yz}, \varpi_{zx}, \varpi_{xy}) = \frac{1}{2} \nabla \times \left( \frac{\gamma \mathbf{v}}{T} \right), \quad (11)$$

one gets for the spin vector

$$S^0(x, p) = \frac{1}{4m} \mathbf{p} \cdot \varpi_S, \quad (12)$$

$$\mathbf{S}(x, p) = \frac{1}{4m} (E_p \varpi_S + \mathbf{p} \times \varpi_T), \quad (13)$$

where  $E_p = \sqrt{\mathbf{p}^2 + m^2}$  is the energy, and  $\mathbf{p}$  is the momentum of  $\Lambda$ .

The spin vector of  $\Lambda$  hyperon measured in the STAR experiment in the local rest frame of  $\Lambda$ , i.e.  $S^{*\mu} = (0, \mathbf{S}^*)$ , is related to that in the center-of-mass frame of Au+Au collisions by a Lorentz boost

$$\mathbf{S}^*(x, p) = \mathbf{S} - \frac{\mathbf{p} \cdot \mathbf{S}}{E_p (m + E_p)} \mathbf{p}. \quad (14)$$

In the transport model calculations we have to average vector  $\mathbf{S}^*$  over all  $\Lambda$ 's emitted from the expanding fireball

$$\langle \mathbf{S}^* \rangle = \frac{1}{N} \sum_{i=1}^N \mathbf{S}^*(x_i, p_i), \quad (15)$$

where  $N$  is the total amount of Lambdas in all events. The global polarization of  $\Lambda$  in the STAR experiment is the projection of averaged spin  $\langle \mathbf{S}^* \rangle$  onto the direction of global angular momentum in non-central collisions [9]

$$P = \frac{\langle \mathbf{S}^* \rangle \cdot \mathbf{J}}{|\langle \mathbf{S}^* \rangle| |\mathbf{J}|}, \quad (16)$$

with  $\mathbf{J}$  being the global orbital angular momentum.

#### 4. Vorticity of nuclear matter and $\Lambda$ , $\bar{\Lambda}$ polarization

We studied Au+Au collisions at c.m. energies corresponding to Beam Energy Scan program at RHIC, ranging from  $\sqrt{s} = 7.7$  to 62.4 GeV. At each energy one million collisions with the impact parameters  $b = 6$  fm and  $b = 9$  fm were generated. - The impact parameters were chosen to compare the results of  $\Lambda$  and  $\bar{\Lambda}$  polarization to the experimental data obtained at centrality  $20\% \leq \sigma/\sigma_{geo} \leq 50\%$ . The kinematic cuts imposed on the  $\Lambda$  and  $\bar{\Lambda}$  spectra match those of the STAR experiment [26] for rapidity,  $|y| \leq 1$ , and transverse momentum,  $0.1 \leq p_T \leq 3$  GeV/c.

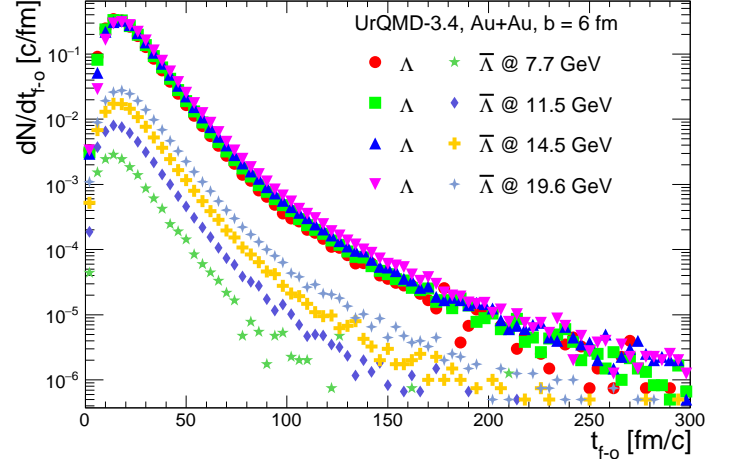


Figure 1: (Color online) Emission functions for  $\Lambda/\bar{\Lambda}$  hyperons in UrQMD calculations of Au+Au collisions with  $b = 6$  fm at  $\sqrt{s} = 7.7$  GeV (circles/stars), 11.5 GeV (squares/diamonds), 14.5 GeV (triangles-up/big crosses), and 19.6 GeV (triangles-down/small crosses).

$\sqrt{s}$ (GeV)	7.7	11.5	14.5	19.6
$\langle t_{FO}^{\Lambda} \rangle$ (fm/c)	21.3009	21.9568	23.066	24.3462
$\langle t_{FO}^{\bar{\Lambda}} \rangle$ (fm/c)	19.7806	21.0302	21.959	23.1288

Table 1: Mean freeze-out time of  $\Lambda$  and  $\bar{\Lambda}$  hyperons in UrQMD calculations of Au+Au collisions with  $b = 6$  fm at  $\sqrt{s} = 7.7 - 19.6$  GeV.

First, one has to study freeze-out conditions of both hyperons, because it is well-known that microscopic transport models demonstrate non-uniform continuous freeze-out of hadrons [35–37] rather than the sharp one. Emission functions  $dN/dt$  for  $\Lambda$  and  $\bar{\Lambda}$  are shown in Fig 1.

Although the main amounts of both hyperons are emitted within 10 - 25 fm/c, there is a continuous radiation of  $\Lambda$  and  $\bar{\Lambda}$  up to very late stage. The mean values of the freeze-out times, listed in Table 1, show that  $\bar{\Lambda}$  hyperons are emitted in average about 1 fm/c earlier than  $\Lambda$ 's. This difference looks insignificantly small, however, the fireball rapidly expands and its temperature drops quickly.

We have to check, therefore, the temperatures of the areas from where the hyperons were emitted. To get the temperature map, the whole space was subdivided into cubic cell with volume  $V = 1$  fm<sup>3</sup>. Then, we calculated the total energy density  $\varepsilon$ , net baryon density  $\rho_B$ , and net strange density  $\rho_S$  as functions of time  $t$  for each cell in its local rest frame. The time step is  $\Delta t = 1$  fm/c. After that, the procedure described in Sec. 2 was employed to find the temperature and the chemical potentials in each cell. Figure 2 displays the distribution of temperature in

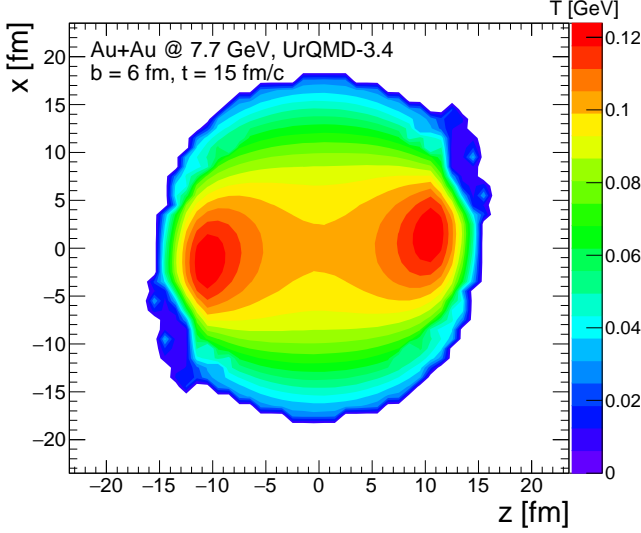


Figure 2: (Color online) Distribution of the proper temperature in the reaction plane in UrQMD calculations of Au+Au collisions with  $b = 6$  fm at  $\sqrt{s} = 7.7$  GeV at  $t = 15$  fm/c.

the reaction plane of Au+Au collisions with  $b = 6$  fm at  $\sqrt{s} = 7.7$  GeV at  $t = 15$  fm/c after beginning of the collision.

One can see that the temperature is not uniformly distributed within the whole volume. Here the spectator areas are the hottest parts of the fireball. The temperature gradually drops from the inner to outer zones. Note again, that this is the proper temperature obtained after the subtraction of collective velocity of each cell. Therefore, the temperatures of emitted hadrons depend both on the emission times and on the location of their freeze-out areas in space. The density distributions of both hyperons in the reaction plane  $d^2N/dxdz$  depicted in Fig. 3 are quite different. Whereas maximum densities of  $\Lambda$  are in the spectator's areas,  $\bar{\Lambda}$  are concentrated mainly in the baryon-less zones. Thus, both  $\Lambda$  and  $\bar{\Lambda}$  are not only frozen, in average, at a bit different times. These hyperons are also emitted from different areas of space with different temperatures.

We are ready now to study vorticity in the system. Of three vorticity components in space, the reaction-plane component  $\varpi_{zx}$  is the most important for calculation of  $\Lambda$  and  $\bar{\Lambda}$  polarization because it is parallel to angular momentum of the system. This vorticity is presented in Fig. 4; the calculations are also done for gold-gold collisions with  $b = 6$  fm at  $\sqrt{s} = 7.7$  GeV and at  $t = 15$  fm/c.

Although  $\varpi_{zx}$  has a quadruple-like structure in  $z - x$  plane, its first and third quadrants are connected by region with small negative vorticity. This connecting part becomes smaller and disappears with increasing collision

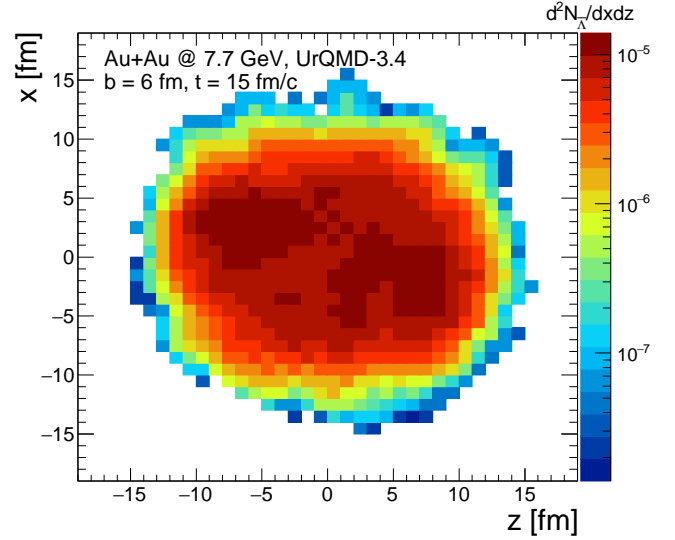
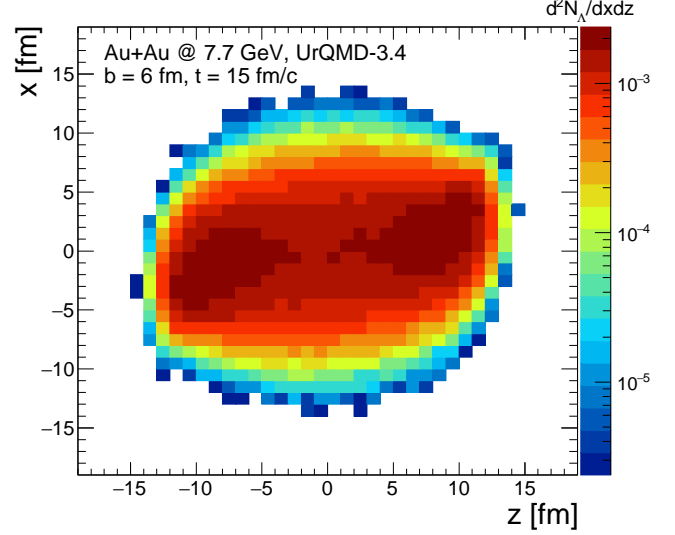


Figure 3: (Color online) Density distributions  $d^2N/dxdz$  of  $\Lambda$  (upper plot) and  $\bar{\Lambda}$  (bottom plot) in the reaction plane in UrQMD calculations of Au+Au collisions with  $b = 6$  fm at  $\sqrt{s} = 7.7$  GeV at  $t = 15$  fm/c.

energy, whereas at lower energies it becomes larger. The structure is stable in time, but the vorticity magnitude decreases due to system expansion. It means that in general the average value of  $\varpi_{zx}$  is negative, thus resulting to positive total polarization. Also, it means that the global polarization of hyperons should decrease with time and with rising energy of the collision. Our result is compatible with other transport model calculations [11] and with hydrodynamic calculations of thermal vorticity [9, 22].

Now we will analyze Lambda and antiLambda hyperons distribution over  $\varpi_{zx}$  at freeze-out point and study their emission functions as functions of both time and  $\varpi_{zx}$ . These functions are displayed in Fig. 5 and Fig. 6 for UrQMD calculations of Au+Au non-central collisions

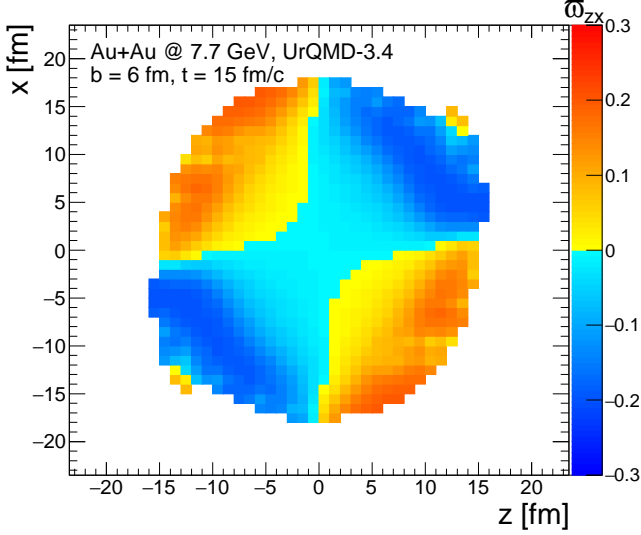


Figure 4: (Color online) Thermal vorticity component  $\varpi_{zx}$  in the reaction plane in UrQMD calculations of Au+Au collisions with  $b = 6$  fm at  $\sqrt{s} = 7.7$  GeV at  $t = 15$  fm/c.

with  $b = 6$  fm at  $\sqrt{s} = 7.7$  GeV and 62.4 GeV, respectively.

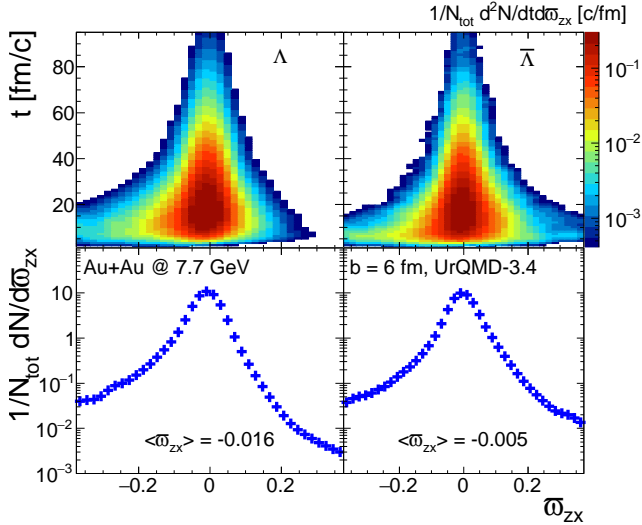


Figure 5: (Color online) Upper row: The emission function of  $\Lambda$  (left) and  $\bar{\Lambda}$  (right) as function of time and  $\varpi_{zx}$  component of vorticity in UrQMD calculations of Au+Au collisions with  $b = 6$  fm at  $\sqrt{s} = 7.7$  GeV. Bottom row: The distribution of  $\Lambda$  (left) and  $\bar{\Lambda}$  (right) over  $\varpi_{zx}$  component of vorticity at the emission point.

At  $\sqrt{s} = 7.7$  GeV  $\Lambda$  and  $\bar{\Lambda}$  are mainly emitted from the regions with small negative vorticity, thus both hyperons have non-zero positive polarization. The distributions of  $\Lambda$  and  $\bar{\Lambda}$  have pronounced maxima shifted to negative values of  $\varpi_{zx}$ . For  $\Lambda$  the maximum is located at  $\varpi_{zx}^\Lambda \approx -0.016$ , whereas for  $\bar{\Lambda}$  the maximum is shifted

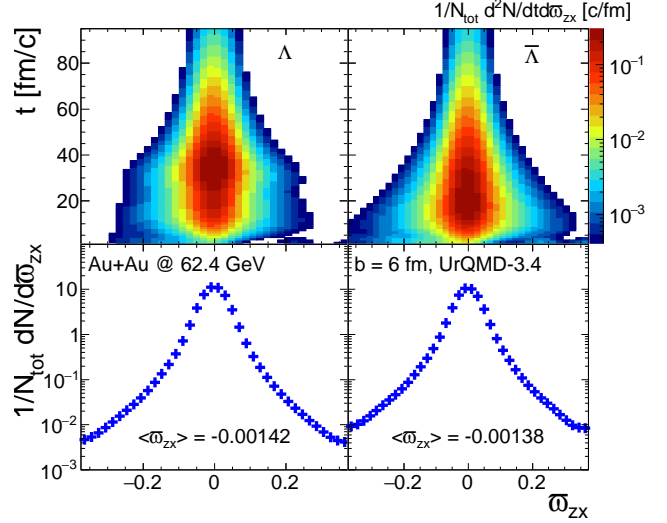


Figure 6: (Color online) The same as Fig. 5, but for  $\sqrt{s} = 62.4$  GeV.

closer to zero,  $\varpi_{zx}^{\bar{\Lambda}} \approx -0.005$ . At  $\sqrt{s} = 62.4$  GeV, shown in Fig. 6, both hyperon species have more symmetric and wide distributions. The positions of their maxima are at  $\varpi_{zx}^{\Lambda/\bar{\Lambda}} \approx -0.0014$ . Emission functions of both  $\Lambda$  and  $\bar{\Lambda}$  show that the main bunch of  $\Lambda$  and  $\bar{\Lambda}$  is decoupled from the system between 7 fm/c and 25 fm/c. The distributions of the later emitted hyperons are more symmetric with respect to  $\varpi_{zx}$  thus implying that the overall hyperon polarization is dominated by early emitted particles.

emission point, one can calculate the global polarization of both hyperon species. Recall that polarization of each hyperon is calculated with Eq.(8) using the thermal vorticity at the space-time point of the hyperon production. Global polarizations of  $\Lambda$  and  $\bar{\Lambda}$  as functions of the emission time are presented in Fig. 7 for energies ranging from  $\sqrt{s} = 7.7$  GeV to  $\sqrt{s} = 62.4$  GeV. Both polarizations quickly drop almost exponentially from 20-60% at very early times to about 0.5% at  $t = 10$  fm/c. After that time the slopes of the distributions become more acclivous. The higher the energy of the collision, the steeper the slopes. The explanation of this effect is rather straightforward. At the very beginning all  $\Lambda$  and  $\bar{\Lambda}$  are formed within the lump of hot and dense matter with high polarization. As the fireball expands, the average vorticity  $\varpi_{zx}$  and polarization in different areas of the fireball decrease rapidly. The larger global polarization at lower bombarding energies originates from the larger production rates of  $\Lambda$  and  $\bar{\Lambda}$  in the negative-vorticity region because of the slower expansion rate of the fireball.

Using the thermal vorticity and momentum of each hyperon at its Energy dependence of the global polariza-



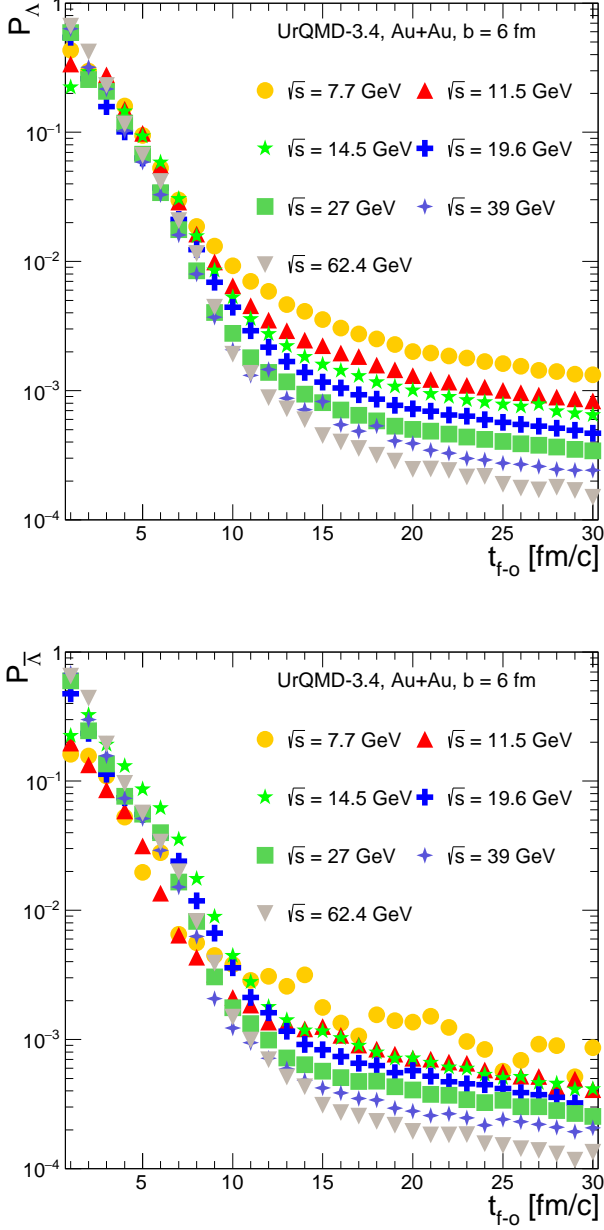


Figure 7: (Color online) Upper plot: Global  $\Lambda$  polarization dependence on the emission time for  $\sqrt{s} = 7.7$  GeV (circles), 11.5 GeV (triangles up), 14.5 GeV (stars), 19.6 GeV (crosses), 27 GeV (squares), 39 GeV (asterisks) and 62.4 GeV (triangles down), respectively. Bottom plot: The same as the upper plot but for  $\bar{\Lambda}$  polarization.

tion of  $\Lambda$  and  $\bar{\Lambda}$  in Au+Au collisions with  $b = 6$  fm and  $b = 9$  fm is displayed in Fig. 8. Here the results of the UrQMD calculations are confronted to the STAR data [26, 38] obtained for the centrality  $20\% \leq \sigma/\sigma_{geo} \leq 50\%$ . We took into account  $\Lambda$  and  $\bar{\Lambda}$  emitted before  $t = 30$  fm/c. For the collisions at energies  $\sqrt{s} \geq 11.6$  GeV the UrQMD results are very close to the data. It is worth mentioning that the fixed impact parameter  $b = 6$  fm corresponds to centrality close to 20%, whereas  $b = 9$  fm roughly corresponds to 45% of centrality. For more peripheral collisions polarization of both hyperons increases. For all energies except  $\sqrt{s} = 7.7$  GeV the difference between the polarizations of  $\Lambda$  and  $\bar{\Lambda}$  in Au+Au collisions with  $b = 9$  fm is at least not smaller than that in collisions with  $b = 6$  fm. The increase of global polarization of both hyperons at lower energies is due to more abundant production of  $\Lambda$  and  $\bar{\Lambda}$  in the negative-vorticity region because of the slow expansion rate. The difference between the global polarization of  $\Lambda$  and  $\bar{\Lambda}$ , clearly seen in experimental data, is correctly reproduced in the model. It is explained by the difference in space-time distributions of  $\Lambda$  and  $\bar{\Lambda}$  and different freeze-out conditions of both hyperons with respect to the thermal vorticity field.

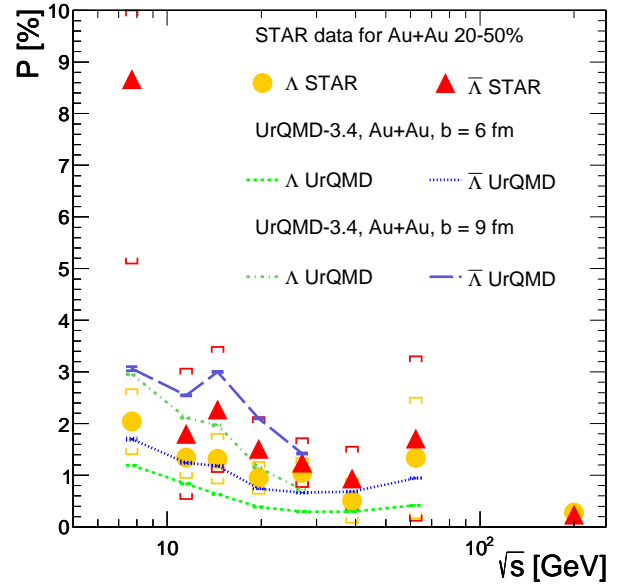


Figure 8: (Color online) Global  $\Lambda$  (dashed line) and  $\bar{\Lambda}$  (dotted line) polarization as function of  $\sqrt{s}$  in UrQMD calculations of Au+Au collisions with  $b = 6$  fm in comparison with the data from STAR experiment [26, 38] (circles and triangles, respectively). Polarization of  $\Lambda$  and  $\bar{\Lambda}$  in Au+Au collisions with  $b = 9$  fm is shown by the dash-dotted and long-dashed lines, respectively.

Note that the polarization of  $\Lambda$  hyperons produced in decays of  $\Sigma^*(1385)$  or  $\Sigma^0(1192)$  was calculated similarly

to the polarization of primarily produced  $\Lambda$ . As shown, e.g., in [12] and [16], the decays of  $\Sigma$  lead to suppression of the global polarization of  $\Lambda$  by about 15-20%. However, the  $\Sigma$  hyperons in microscopic transport calculations possess the thermal vorticity of the cell they were produced or experienced the last interaction before the decay to  $\Lambda + \pi$  for  $\Sigma^*$  or  $\Lambda + \gamma$  for  $\Sigma^0$ . This vorticity is larger than the thermal vorticity of the cell where the decay of  $\Sigma$  takes place. We checked the interplay of both effects for Au+Au collisions with  $b = 6$  fm at  $\sqrt{s} = 7.7$  GeV. The overall correction to global  $\Lambda$  polarization was found to be about 4%, i.e., quite small. The detailed study of this interplay for other energies and impact parameters will be done in a forthcoming publication.

The model cannot match only the magnitude of  $\bar{\Lambda}$  polarization measured at  $\sqrt{s} = 7.7$  GeV. Here the polarization of both hyperons in collisions with  $b = 9$  fm increases to approximately 3%, see Fig. 8. Note, however, that the yield of  $\bar{\Lambda}$  in peripheral Au+Au collisions at this energy is very low. Thus, the relatively modest value of  $\bar{\Lambda}$  polarization can be caused by unfortunate statistical fluctuation. Another plausible solution is to increase slightly the number of antilambdas emitted within first 10 fm/c. The sudden rise of  $\bar{\Lambda}$  polarization at low energies deserves further investigations.

## 5. Conclusions

We calculated thermal vorticity in Au+Au collisions with  $b = 6$  fm at beam energy scan energies  $7.7 \leq \sqrt{s} \leq 62.4$  GeV within the UrQMD model. Statistical model of ideal hadron gas was used to extract the temperature of the space areas from where both  $\Lambda$  and  $\bar{\Lambda}$  were emitted. Quadruple structure of  $\varpi_{zx}$  component of vorticity is obtained, and dependence of  $\varpi_{zx}$  on time and energy is studied.

It was found that freeze-out conditions of  $\Lambda$  and  $\bar{\Lambda}$  are different both in space and in time. This means, particularly, that the studied hyperons are emitted from parts of the fireball with different thermal vorticity.

Method for calculation of  $\Lambda$  and  $\bar{\Lambda}$  global polarization in transport model is developed. Using this method  $\Lambda$  and  $\bar{\Lambda}$  global polarization is calculated in Au+Au collisions at energies  $\sqrt{s} = 7.7 - 62.4$  GeV and compared with the data from STAR experiment. Polarization of  $\Lambda$  and  $\bar{\Lambda}$  decreases with increasing collision energy in line with the experimental data.

It was found that within the thermal approach the global polarization in transport models is jointly determined by the space-time distribution of  $\Lambda/\bar{\Lambda}$  and the thermal vortic-

ity field. The larger global polarization at lower collision energies is due to larger production rate of the hyperons in the negative-vorticity region because of the slow expansion rate. This means that the magnitude of vorticity decreases slower than at higher collision energies.

For the first time, the difference between global polarization of  $\Lambda$  and  $\bar{\Lambda}$  is obtained within the thermal approach. This difference is naturally explained by the difference in space-time distributions of  $\Lambda$  and  $\bar{\Lambda}$  and different freeze-out with respect to the thermal vorticity field.

**Acknowledgments.** The authors are grateful to L. Csernai, Yu. Ivanov, A. Sorin and O. Teryaev for fruitful discussions and valuable comments. The work of L.B. and E.Z. was supported by Russian Foundation for Basic Research (RFBR) under Grants No. 18-02-40084 and No. 18-02-40085, and by the Norwegian Research Council (NFR) under Grant No. 255253/F50 - "CERN Heavy Ion Theory". O.V. acknowledges the financial support of the Norwegian Centre for International Cooperation in Education (SIU) under Grant "CPEA-LT-2016/10094 - From Strong Interacting Matter to Dark Matter". All computer calculations were made at Abel (UiO, Oslo) and Govorun (JINR, Dubna) computer cluster facilities.

## References

- [1] *Proc. of Quark Matter 2019* edited by F. Antinori, A. Dainese, P. Giubellino et al., Nucl. Phys. A 982 (2019) pp. 1-1066.
- [2] Z. Liang, X.N. Wang, Phys. Rev. Lett. 94 (2005) 102301; Erratum ibid. 96 (2006) 039901(E).
- [3] F. Becattini, F. Piccinini, J. Rizzo, Phys. Rev. C 77 (2008) 024906.
- [4] O. Rogachevsky, A. Sorin, O. Teryaev, Rhys. Rev. C 82 (2010) 054910.
- [5] X.G. Huang, P. Huovinen, X.N. Wang, Phys. Rev. C 84 (2011) 054910.
- [6] J.H. Gao, Z.T. Liang, S. Pu, Q. Wang, X.N. Wang, Phys. Rev. Lett. 109 (2012) 232301.
- [7] F. Becattini, V. Chandra, L. Del Zanna, E. Grossi, Ann. Phys. (NY) 338 (2013) 32.
- [8] F. Becattini, L.P. Csernai, D.J. Wang, Phys. Rev. C 88 (2013) 034905; Erratum: ibid. 93 (2016) 069901.
- [9] F. Becattini et al., Eur. Phys. J. C 75 (2015) 406.
- [10] L.G. Pang, H. Petersen, Q. Wang, X.N. Wang, Phys. Rev. Lett. 117 (2016) 192301.
- [11] H. Li, L.G. Pang, Q. Wang, X.L. Xia, Phys. Rev. C 96 (2017) 054908.
- [12] F. Becattini et al., Phys. Rev. C 95 (2017) 054902.
- [13] A. Sorin, O. Teryaev, Phys. Rev. C 95 (2017) 011902(R).
- [14] M. Baznat, K. Gudima, A. Sorin, O. Teryaev, Phys. Rev. C 95 (2017) 011902.
- [15] Y. Xie, D. Wang, L.P. Csernai, Phys. Rev. C 95 (2017) 031901.
- [16] I. Karpenko, F. Becattini, Eur. Phys. J. C 77 (2017) 213.
- [17] Y.B. Ivanov, A.A. Soldatov, Eur. Phys. J. A 52 (2016) 367.
- [18] Y.B. Ivanov, A.A. Soldatov, Phys. Rev. C 95 (2017) 054915.

- [19] E.E. Kolomeitsev, V.D. Toneev, V. Voronyuk, Phys. Rev. C 97 (2018) 064902.
- [20] Y.B. Ivanov, A.A. Soldatov, Phys. Rev. C 97 (2018) 021901.
- [21] L.P. Csernai, J.I. Kapusta, T. Welle, Phys. Rev. C 99 (2019) 021901.
- [22] Y.B. Ivanov, V.D. Toneev, A.A. Soldatov, Phys. Rev. C 100 (2019) 014908.
- [23] Y.B. Ivanov, V.D. Toneev, A.A. Soldatov, arXiv:1910.01332 [nucl-th].
- [24] B. Abelev et al. (STAR Collaboration), Phys. Rev. C 76 (2007) 024915.
- [25] S. Acharya et al. (ALICE Collaboration), arXiv:1909.01281 [nucl-ex].
- [26] L. Adamczyk et al. (STAR Collaboration), Nature 548 (2017) 62.
- [27] S.A. Bass et al., Prog. Part. Nucl. Phys. 41 (1998) 255.
- [28] M. Bleicher et al., J. Phys. G: Nucl. Part. Phys. 25 (1999) 1859.
- [29] L.V. Bravina et al., Phys. Lett. B 434 (1998) 379.
- [30] L.V. Bravina et al., J. Phys. G 25 (1999) 351.
- [31] L.V. Bravina et al., Phys. Rev. C 60 (1999) 024904.
- [32] L.V. Bravina et al., Phys. Rev. C 63 (2001) 064902.
- [33] L.V. Bravina et al., Phys. Rev. C 78 (2008) 014907.
- [34] D. Oliinychenko, H. Petersen, Phys. Rev. C 93 (2016) 034905.
- [35] S.A. Bass et al., Phys. Rev. C 60 (1999) 021902.
- [36] L.V. Bravina et al., Phys. Lett. B 354 (1995) 196.
- [37] L.V. Bravina et al., Phys. Rev. C 60 (1999) 044905.
- [38] J. Adam et al. (STAR Collaboration), Phys. Rev. C 98 (2018) 014910.